Applied Catalysis B: Environmental 181 (2016) 475–480

Contents lists available at ScienceDirect

Applied Catalysis B: Environmental

journal homepage: www.elsevier.com/locate/apcatb

Photocatalytic decomposition of various organic compounds over WO_3-supported ordered intermetallic PtPb co-catalysts

Takao Gunji [a], Arockiam John Jeevagan [a], Masanari Hashimoto [a], Toshiaki Nozawa [a], Toyokazu Tanabe [a], Shingo Kaneko [b], Masahiro Miyauchi [c], Futoshi Matsumoto [a,*]

[a] Department of Material and Life Chemistry, Kanagawa University, 3-27-1, Rokkakubashi, Kanagawa-ku, Yokohama, Kanagawa 221-8686, Japan
[b] Research Institute for Engineering, Kanagawa University, 3-27-1, Rokkakubashi, Kanagawa-ku, Yokohama, Kanagawa 221-8686, Japan
[c] Department of Metallurgy and Ceramic Science, Graduate School of Science and Engineering, Tokyo Institute of Technology, 2-12-1 Ookayama, Meguro-ku, Tokyo 152-8552, Japan

ARTICLE INFO

Article history:
Received 2 June 2015
Received in revised form 5 August 2015
Accepted 9 August 2015
Available online 11 August 2015

Keywords:
Photocatalyst
Intermetallic PtPb co-catalyst
Visible light
Quantum efficiency
Reaction mechanism

ABSTRACT

This study investigates the photocatalytic decomposition of acetic acid and its reaction mechanism over WO_3-supported ordered intermetallic PtPb nanoparticle (NiAs-type structure, P63/mmc, $a = 0.4259$ nm; $c = 0.5267$ nm) (PtPb NPs/WO_3) co-catalysts under an oxygen-rich atmosphere and visible light. We rationally designed and synthesized the ordered intermetallic nanoparticle on WO_3 co-catalysts by a photodeposition and polyol method. Remarkably enhanced activities were observed for the synthesized PtPb NPs/WO_3 catalyst toward the decomposition of organic compounds compared to pure WO_3 and WO_3-supported individual Pt co-catalysts.

1. Introduction

In recent years, semiconductor photocatalysts such as TiO_2 and WO_3 have gained attention for applications in environmental remediation [1], H_2 evolution [2], water splitting [3], and CO_2 reduction [4]. Photocatalysts that are active in the visible light region can be very useful as they efficiently decompose harmful organic compounds such as acetic acid (AcOH), acetaldehyde, and formaldehyde under indoor light or sun-light [5,6]. In particular, WO_3 has attracted considerable interest because of its visible light-responsive properties and deeper holes in its valence band. However, WO_3 by itself cannot be used as a photocatalyst because of its lower conduction band (CB) edge. The CB level of WO_3 (+0.50 V vs. NHE) is slightly negative compared with the potential for the multi-electron reduction of oxygen ($O_2/H_2O_2 = 0.68$ V vs. NHE) [7]. The oxygen in WO_3 lacks the ability to scavenge CB electrons that causes the recombination rate of electrons and holes to increase, resulting in a significant decline in photocatalytic activity. Therefore, in order to improve the photocatalytic efficiency of WO_3 for decomposing organic compounds, WO_3 requires a co-catalyst on its surface to facilitate oxygen reduction reactions (ORR). Recently, Abe et al. reported that Pt nanoparticle-loaded (1 wt.%) WO_3 (Pt NPs/WO_3) photocatalysts effectively decomposed organic compounds under visible light and full arc in an oxygen-rich atmosphere [8]. This indicated that the surface of the Pt NPs facilitates oxygen reduction on WO_3. We have previously reported that ordered intermetallic PtPb NPs exhibit efficient electrocatalytic activity for the oxidation of formic acid, methanol (MeOH), and ethanol [9]. In our recent study, we demonstrated that ordered intermetallic PtPb NPs on TiO_2 electrochemically accelerated ORR in acidic media [10]. In addition, we found that $H_2PtCl_6{\cdot}6H_2O$ and $Pb(CH_3COO)_2$ can be co-reduced using sodium borohydride to precipitate PtPb NPs (average particles size: 9.5 nm) over the WO_3 support (PtPb NPs/WO_3). PtPb NPs/WO_3 showed substantial photocatalytic activity toward the decomposition of AcOH in aqueous solutions [11]. However, its photocatalytic activity was not sufficient with this method because the nanoparticle size was not controlled and the details of the photocatalytic reaction mechanism of PtPb NPs/WO_3 were not disclosed.

The investigations suggested that the construction of ordered intermetallic PtPb NPs as co-catalysts for photocatalysis on WO_3 could potentially increase the photocatalytic activity. Herein, we report the synthesis of PtPb NPs/WO_3 via a photodeposition and polyol method to control the particle size and demonstrate

* Corresponding author. Fax: +81 45 413 9770.
E-mail address: fmatsumoto@kanagawa-u.ac.jp (F. Matsumoto).

http://dx.doi.org/10.1016/j.apcatb.2015.08.016
0926-3373/

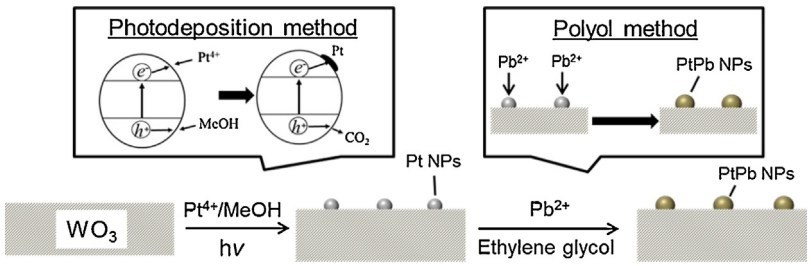

Scheme 1. Schematic representation of Pt NPs and ordered intermetallic PtPb NPs loading on WO_3 using two step synthesis method.

enhanced photocatalytic activity toward the decomposition of various organic compounds. The product is compared to pure WO_3 and Pt NPs/WO_3 toward the photocatalytic decomposition of various organic compounds. In addition, we discuss how co-catalysts contribute in enhancing the decomposition of organic compounds under visible light irradiation.

2. Experimental

2.1. Preapration of PtPb loaded WO_3 photocatalyst

A two-step synthesis method for the formation of WO_3-supported ordered intermetallic PtPb NPs is shown in Scheme 1. Pt (1 wt.%) NPs/WO_3 was used as a starting material for the synthesis of ordered intermetallic PtPb NPs/WO_3. In the first step, Pt NPs/WO_3 was synthesized through a photodeposition method reported by Abe et al. [8]. In the second step, the synthesized Pt NPs/WO_3 (0.4 g) was dispersed in ethylene glycol (50 mL) in the presence of $Pb(CH_3COO)_2$ (0.03 mmol), and then potassium hydroxide (1 mg) was added to the mixture. The mixture was sonicated for 20 min in a bath-type sonicator. The mixture was then refluxed for 6 min under a microwave (Focused microwave instrument, CEM) power of 300 W. After cooling, the PtPb NPs/WO_3 was collected by centrifugation, washed with ethanol, and finally dried under vacuum.

2.2. Characterization

X-ray photoelectron spectroscopy (XPS) measurements (JEOL, JP-9010 MC) were performed to examine the chemical states (Pt 4*f* and Pb 4*f*) of the catalyst. MgKα as X-ray source with anodic voltage (10 kV) and current (10 mA) were used for XPS measurements. All XPS spectra of the samples were obtained with a take-off angle at 45° with respect to the specimens by using the pass energies of 100 eV and 200 eV for narrow and survey scans, respectively. We used a 200 kV transmission electron microscope (TEM and/or STEM, JEM-2100F, JEOL) equipped with two aberration correctors (CEOS GmbH) for the image- and probe-forming lens systems and an X-ray energy-dispersive spectrometer (JED-2300T, JEOL) for compositional analysis. Both the aberration correctors were optimized to realize the point-to-point resolutions of TEM and scanning transmission electron microscopy (STEM) as 1.3 and 1.1 Å, respectively. A probe convergence angle of 29 mrad and a high-angle annular-dark-field (HAADF) detector with an inner angle greater than 100 mrad were used for HAADF-STEM observation. The samples for TEM were prepared by dropping a methanol suspension of the sample powder onto a commercial TEM grid coated with a collodion film. The sample was thoroughly dried in vacuum prior to observation. The UV–vis experiments were conducted on a UV-2600 (Shimadzu) double beam spectrometer with an integration sphere diffuse reflectance attachment. The powder samples were measured from 300 to 800 nm. Powder X-ray diffractometry (pXRD) was performed using CuKα radiation (Rigaku RINT-Ultima III; λ = 0.1548 nm) with an increment of 0.02° in a range of diffraction angles from 20 to 80°. An obliquely finished Si crystal (non-reflection Si plate) was used as a sample holder to minimize the background.

2.3. Evaluation of the decomposition rate of AcOH with Pt NPs/WO_3 and PtPb NPs/WO_3

The photocatalytic decomposition of AcOH was carried out in a circulation system made of Pyrex, in which a suspension of the photocatalyst powder (200 mg) in an aerated aqueous AcOH solution (5 vol%, 300 mL) was continuously stirred using a magnetic stirrer. A 300 W Xe lamp was used as the light source. The components were analyzed in the gas phase by gas chromatography (GC-8A, Shimadzu) equipped with a 2 m Porapak-Q column, a 2 m molecular sieve 3× column, and a flame ionisation detector while using Ar as the carrier gas. The sample was illuminated with a 300 W Xe lamp (PE-300BF, BA-X300ES, Hayashi Tokei Works Co., Ltd., Japan) in conjunction with an optical fiber coupler, UV cut-off filter (L-42, HOYA Co., Ltd., Japan), and an IR cut-off filter (MR5090/CM). A spectro-radiometer (USR-45D, Ushio Co.) measured the visible light intensity, which was adjusted to 20 mW cm^{-2}.

3. Results and discussion

Fig. 1 shows the XPS profiles for the (A) W 4*f* and (B) Pt 4*f* regions of (a) PtPb NPs/WO_3 and (b) WO_3, respectively. Fig. 1A shows the XPS profiles in the W 4*f* region for bulk WO_3 and PtPb NPs/WO_3 as references. Spectra (a) and (b) shown in Fig. 1A show two peaks, 37.8 and 35.6 eV, assigned to W^{6+}. This result was significantly different from our previous study using sodium borohydride as a reducing agent [11]. The spectra suggest that the oxidation state of W does not change from the original state of WO_3 after reduction by ethylene glycol. The XPS profiles shown in Fig. 1B represent the Pt 4*f* regions for the (a) ordered intermetallic PtPb, (c) reference bulk PtPb, and (d) bulk Pt NPs. The Pt 4*f* peaks in the bulk PtPb spectra were shifted to a higher binding energy level (by +0.3 eV) than that of bulk Pt. The Pt 4*f* peaks in PtPb NPs/WO_3 corresponded to Pt 4*f* in the bulk PtPb peaks. This indicated that the Pb ions were reduced on the Pt NP sites of WO_3 and could form intermetallic compounds with the same chemical composition as bulk PtPb.

Fig. 2 shows the diffuse reflectance UV–vis absorption spectra for pure WO_3, Pt NPs/WO_3 and PtPb NPs/WO_3. The absorption edges of the synthesized Pt NPs/WO_3 and PtPb NPs/WO_3 sample are closely matched with pure WO_3. This result indicates that Pt NPs/WO_3 and PtPb NPs/WO_3 samples had ability to absorb visible light as like pure WO_3.

Fig. 3 shows the pXRD patterns of PtPb NPs/WO_3 (Pt loading on WO_3: 1 wt.% and 4 wt.%). It is clear that, when the amount of PtPb is 1 wt.%, no distinct peaks of PtPb in the PtPb NPs/WO_3 sample was found because of the PtPb NPs peak on PtPb NPs/WO_3 was much small in low loading amount (1 wt.%). However, we observed corresponding PtPb peak in PtPb NPs/WO_3 on high loading amount (4 wt.%) of PtPb NPs.

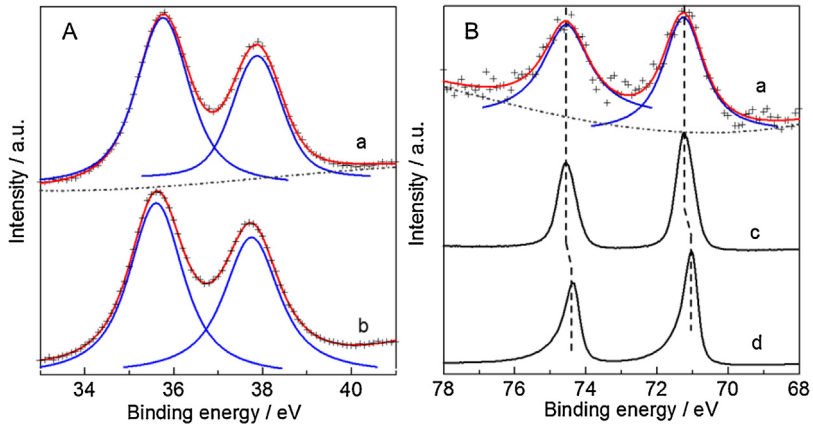

Fig. 1. XPS profiles in the (A) W 4f and (B) Pt 4f regions for (a) PtPb NPs/WO_3 (Pt loading: 1 wt.%), (b) WO_3, (c) bulk PtPb, and (d) bulk Pt.

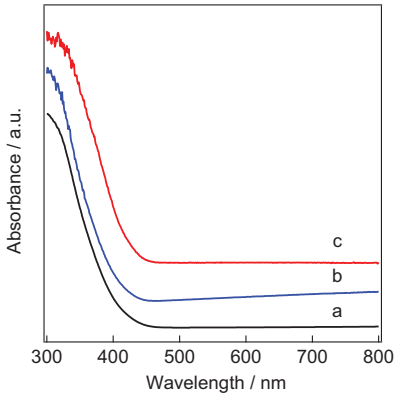

Fig. 2. Diffuse reflectance UV–vis absorption spectra of (a) pure WO_3, (b) Pt NPs/WO_3 and (c) PtPb NPs/WO_3 (b, c: Pt loading on WO_3: 1 wt.%).

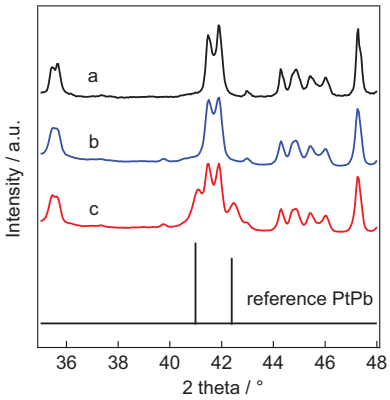

Fig. 3. pXRD diffractograms of (a) pure WO_3, (b) PtPb NPs/WO_3 (Pt loading on WO_3: 1 wt.%) and (c) PtPb NPs/WO_3 (Pt loading on WO_3: 4 wt.%).

Fig. 4A shows a transmission electron microscopy (TEM) image of PtPb NPs/WO_3. The PtPb NPs attached to WO_3 appear as dark spots. The TEM images revealed that the average particle diameter of the ordered intermetallic PtPb NPs on the WO_3 surface was 5.6 nm, which was larger than the photodeposited Pt NPs (average diameter: 3.8 nm for photodeposited Pt NPs) on the WO_3 surface (see Fig. S1). Furthermore, this result implies that the Pb ions may site-selectively react with the Pt NPs immobilized on the WO_3 sur-

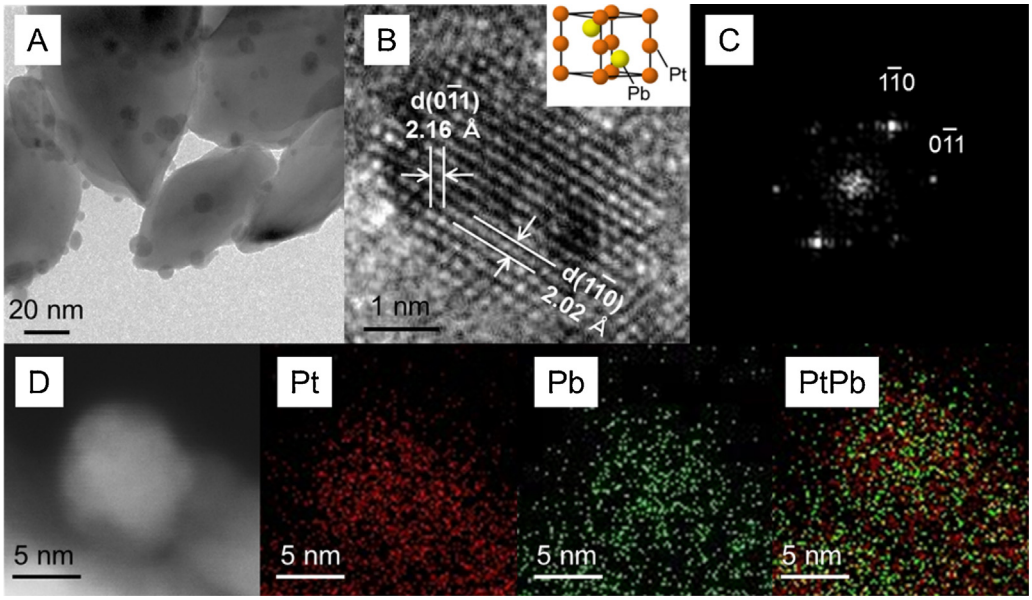

Fig. 4. (A) TEM and (B) HR-TEM images of PtPb NPs/WO_3 (Pt loading: 1 wt.%). (C) FFT pattern obtained from (B). (D) HAADF-STEM image of PtPb NPs/WO_3 and corresponding mapping images. Inset shows the simulated atomically ordered intermetallic PtPb.

face. A high-resolution TEM (HR-TEM) image and its corresponding fast-Fourier transformation (FFT) pattern for the PtPb NPs in PtPb NPs/WO_3 are shown in Fig. 4B and C. The PtPb phase clearly shows two kinds of lattice fringes in which the PtPb NPs have atomically ordered structures on the WO_3 surface. The *d* lattice fringes of the NPs shown in the HR-TEM image are 0.216 and 0.202 nm (Fig. 4B), respectively. This is quite similar to that of the (1 1 0) and (0 1 1) phase of an ordered intermetallic PtPb phase (Fig. 4C). Fig. 4D shows a scanning transmission electron microscopy (STEM) image and compositional mapping with an HAADF-STEM of the PtPb NPs. From the data, it was determined that the Pt and Pb atoms were uniformly dispersed in the particles and that the Pt and Pb molar ratio was 67:33. As shown in Figs. 1–4, Pb precipitation on Pt NPs can site-selectively occur to form individually isolated PtPb NPs on the WO_3 supports. Thus, we succeeded in forming ordered intermetallic compounds of PtPb NPs by photodeposition and polyol methods.

The photocatalytic activity of WO_3, Pt NPs/WO_3, and PtPb NPs/WO_3 was examined for the decomposition of AcOH. The CO_2 evolution during decomposition of AcOH over the WO_3 (black), Pt NPs/WO_3 (blue), and PtPb NPs/WO_3 (red) photocatalysts under visible light irradiation is shown in Fig. 5A. WO_3 shows poor CO_2 generation without Pt or PtPb co-catalysts. Conversely, the photocatalytic activity of WO_3 was enhanced significantly when loaded with Pt NPs. Furthermore, the highest yield of CO_2 evolution was observed with PtPb NPs/WO_3. The amount of CO_2 generation at 5 h for PtPb NPs/WO_3 was 6.4 times more than that for Pt NPs/WO_3. In addition, the CO_2-generation rate at 0–5 h with the PtPb NPs/WO_3 (575.2 $\mu mol\ h^{-1}$) was much higher than that of the Pt NPs/WO_3 (66.5 $\mu mol\ h^{-1}$) and WO_3 (19.6 $\mu mol\ h^{-1}$). Furthermore, the apparent quantum efficiency (QE) of PtPb NPs/WO3 for CO_2 generation from AcOH was 23%, whereas that of Pt (1 wt.%) NPs/WO_3 was 7.3% (Fig. 5A inset). The apparent QE of Pt NPs/WO_3 and PtPb NPs/WO_3 were determined as four- and two-electron reactions, respectively (see Supplementary material, for the detail of QE). The QE was calculated using the rate-limiting light amount. The QE of PtPb NPs/WO_3 was much higher than that of Pt NPs/WO_3 despite its two-electron reaction. Abe et al. also reported that the apparent QE for the decomposition of AcOH with Pt NPs/WO_3 was approximately 10% [6,8]. In addition, the PtPb NPs in PtPb NPs/WO_3 were stable even after 5 h of measurements and the photocatalytic activity did not change even after reuse (see Supplementary material, STEM and STEM-EDS mapping profiles and XPS after the reaction of PtPb NPs/WO_3 (Figs. S2 and 3). Fig. S4 shows stability tests for the photocatalytic activity of AcOH decomposition with PtPb NPs/WO_3).

The ordered intermetallic PtPb NPs/WO_3 exhibited enhanced photocatalytic activity toward AcOH decomposition. This can be explained by the difference in the decomposition mechanism of AcOH between the Pt and PtPb NPs. In considering the AcOH decomposition reaction mechanism, we have determined the amount of H_2O_2 produced from ORR by the co-catalyst. The redox reactions co-instantaneously proceed in the photocatalytic reaction. When using WO_3 as a supporting material to decompose AcOH, multi-electron reduction reaction of oxygen (O_2/H_2O_2 = 0.68 V, O_2/H_2O = 1.23 V vs. NHE) proceeds on the reduction sites because the single-oxygen reduction reaction (O_2/HO_2^- = −0.13 V, O_2/O_2^- = −0.56 V vs. NHE) was more negative than the CB level of pure WO_3 (+0.5 V vs. NHE). H_2O_2 was produced as a product of the two-electron reduction of oxygen on the Pt and/or PtPb NP co-catalysts. When Pt NPs are used as the co-catalyst on WO_3 for decomposing AcOH, CO_2 was not produced in a short timeframe (within 30 min); in such a reaction, H_2O_2 was generated on the reduction sites (see Supplementary material, decomposition of AcOH over Pt NPs/WO_3, Fig. S5). In addition, CO_2 and H_2O_2 were the only reaction products observed. These results indicate that CO_2 was not directly produced when AcOH was decomposed with the Pt NP co-catalysts. Accordingly, the following reaction mechanism is proposed:

$$H_2O + h^+ \rightarrow H^+ + {}^\bullet OH \quad (1)$$

$$CH_3COOH + h^+ \rightarrow {}^\bullet CH_2COOH + H^+ \quad (2)$$

$${}^\bullet CH_2COOH + {}^\bullet OH \rightarrow HOCH_2COOH \quad (3)$$

$$HOCH_2COOH + h^+ \rightarrow {}^\bullet CHOHCOOH + H^+ \quad (4)$$

$${}^\bullet CHOHCOOH + h^+ \rightarrow OHCCOOH + H^+ \quad (5)$$

$$OHCCOOH + {}^\bullet OH + h^+ \rightarrow HOOCCOOH + H^+ \quad (6)$$

$$HOOCCOOH + 2h^+ \rightarrow 2CO_2 + 2H^+ \quad (7)$$

CO_2 was formed through several oxidation reactions when using Pt NPs as co-catalysts. The α-carbon of AcOH was oxidized from the methyl group to the carboxyl group (Eqs. (2)–(6)). H_2O_2 evolution from the reduction reactions in a short timeframe suggests that the oxidation reactions also proceeded. However, CO_2 generation was not observed during this timeframe because of the sequential oxidation of the methyl group. Glycolic acid (Eq. (3)) and glyoxylic acid (Eq. (5)) could not be analyzed because of chemisorption onto the Pt co-catalyst. Eventually, CO_2 was generated through the oxidation of oxalic acid (Eqs. (6) and (7)). In fact, no C—C bond could be cleaved until the formation of oxalic acid.

Decomposition of AcOH on the Pt and PtPb NP co-catalysts proceeds via different mechanisms. In contrast to the Pt NPs, the PtPb NPs generate CO_2 in a short period (within 10 min) (see Supplementary material, decomposition of AcOH over PtPb NPs/WO_3, Fig. S6). In addition, other products were analyzed for considering the reaction mechanism with the PtPb NP co-catalysts. MeOH and ethane were analyzed using PtPb NPs as co-catalysts for AcOH decomposition (Fig. 5C and D). Accordingly, we propose the following reaction mechanism:

$$H_2O + h^+ \rightarrow H^+ + {}^\bullet OH \quad (8)$$

$$CH_3COOH + h^+ \rightarrow {}^\bullet CH_3 + CO_2 + H^+ \quad (9)$$

$${}^\bullet CH_3 + {}^\bullet OH \rightarrow CH_3OH \quad (10)$$

$${}^\bullet CH_3 + {}^\bullet CH_3 \rightarrow CH_3CH_3 \quad (11)$$

$$CH_3OH + h^+ \rightarrow {}^\bullet CH_2OH + H^+ \quad (12)$$

$${}^\bullet CH_2OH + h^+ \rightarrow HCOH + H^+ \quad (13)$$

$$HCOH + {}^\bullet OH + h^+ \rightarrow HCOOH + H^+ \quad (14)$$

$$HCOOH + 2h^+ \rightarrow CO_2 + 2H^+ \quad (15)$$

Unlike the Pt NPs co-catalysts, CO_2 formed during AcOH decomposition with PtPb NPs because C—C bonds were cleaved in the initial process (Eq. (9)). Pb might act as a surface modifier to mediate interactions between the co-catalyst and AcOH and accelerate the photochemical cleavage of C—C bonds. Evidently, CO_2 was detected when H_2O_2 was formed on the reduction sites. Methane radicals were formed as radical intermediates because MeOH and ethane were produced. In order to cleavage C—C bond, radical intermediate has to be stably-formed on catalyst. Pb atom in ordered intermetallic PtPb was strongly contributed a stabilization of methane radical when compared with pure Pt co-catalyst. Formaldehyde and formic acid were not detected because the decomposition of AcOH proceeded rapidly than that of MeOH.

The PtPb NPs are thought to work as co-catalysts for reduction of O_2 and oxidative decomposition of AcOH on the surface on WO_3 based on our previous works and present results [10]. Although the PtPb NPs are formed in the reduction sites because the Pt NPs were formed by the electron excited by absorbing visible light and the PtPb NPs was formed by reacting Pb atoms with the Pt NPs, the surface of PtPb NPs would become both sites where electrons and holes

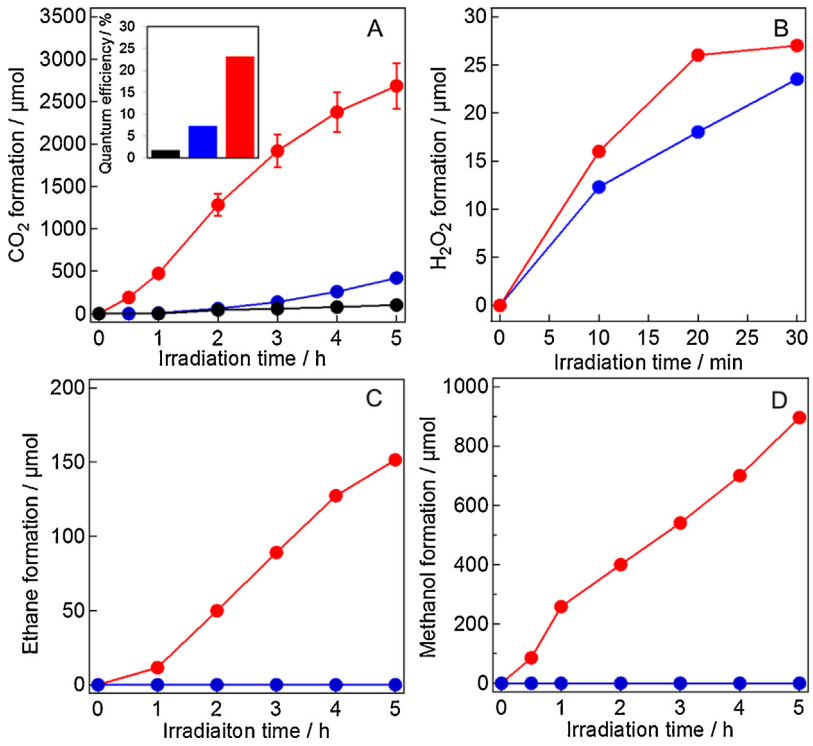

Fig. 5. Time course of (A) CO_2, (B) H_2O_2, (C) ethane and (D) methanol evolution during the decomposition of AcOH over WO_3 (black), Pt NPs/WO_3 (blue) (Pt loading: 1 wt.%) and PtPb NPs/WO_3 (red) (Pt loading: 1 wt.%) photocatalysts suspended in an aqueous AcOH solution in the presence of O_2 under visible light irradiation ($\lambda > 420$ nm). Insets (A): Quantum efficiency of the corresponding decomposition of AcOH. (For interpretation of the references to color in this figure legend, the reader is referred to the web version of this article.)

formed by absorbing visible light are consumed. On the surface of WO_3 which does not exhibit preferential orientation (Fig. 1A) and has low degree of the crystallinity, it could be considered that the reduction and oxidation sites are fixed on the WO_3 surface and shift the position depending on the situation. The photochemical cleavage of CC bonds which is characteristic phenomena in the PtPb NPs/WO_3 is produced by catalytic activity of the PtPb NPs. When Pb ions are reduced with polyol, the question whether Pb atoms are deposited on only the Pt NPs or not is significantly important for the interpretation of the reaction mechanism. We confirmed that Pb ions were not reduced by an individual action of polyol and Pb ions were reduced catalytically on the Pt surfaces by polyol. However, the possibility that cluster of Pb is deposited on the WO_3 surface cannot be denied. The Pb cluster would become Pb oxide cluster in the photocatalytic activity tests. We positively formed the PbO_2 NPs on the WO_3 surfaces with Pb ions and holes formed by absorbing visible light on the WO_3 to check the contribution of PbO_2 NPs to the photochemical cleavage of CC bonds. The Pt NPs/PbO_2 NPs/WO_3 could not exhibit the photo-chemical cleavage of CC bonds. We concluded that origin of the photochemical cleavage of CC bonds is the surface of PtPb NPs and is not the surface of PbO_2 NPs.

Fig. 6A and B shows the oxidation of formaldehyde and MeOH with various photocatalysts (see Supplementary material, decomposition of formaldehyde and MeOH over Pt NPs/WO_3, Fig. S7). When using WO_3 without Pt or PtPb NP co-catalysts, the decomposition of formaldehyde and MeOH did not proceed. In contrast, CO_2 was produced in the decomposition of formaldehyde and MeOH with the co-catalysts. The CO_2-generation rate in the oxidation of formaldehyde with PtPb NPs/WO_3 at 0–5 h was 12.6 times higher

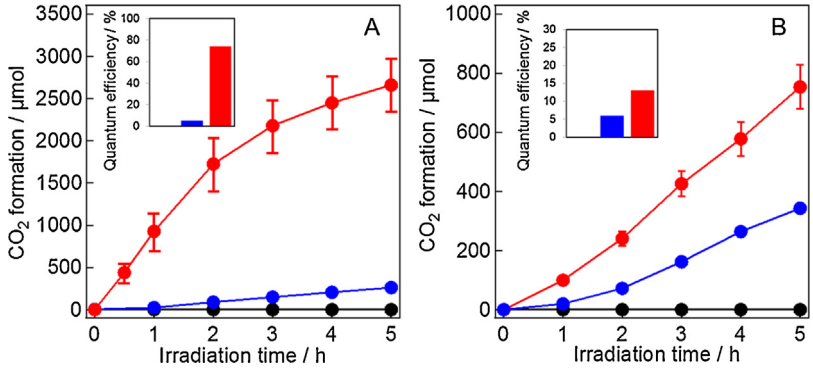

Fig. 6. Time course of CO_2 evolution during the decomposition of (A) formaldehyde and (B) MeOH over WO_3 (black), Pt NPs/WO_3 (blue) (Pt loading: 1 wt.%) and PtPb NPs/WO_3 (red) (Pt loading: 1 wt.%) photocatalysts suspended in an aqueous formaldehyde or MeOH solution in the presence of O_2 under visible light irradiation ($\lambda > 420$ nm). Insets: Quantum efficiency of the corresponding decomposition of formaldehyde or MeOH. (For interpretation of the references to color in this figure legend, the reader is referred to the web version of this article.)

than that with Pt NPs/WO_3 (Fig. 6A). For MeOH oxidation, the CO_2-generation rate with PtPb NPs/WO_3 at 0–5 h was 11.3 times higher than that with Pt NPs/WO_3 (Fig. 6B). In addition, the apparent QEs of formaldehyde and MeOH with PtPb NPs/WO_3 for CO_2 generation were 74% and 13%, respectively. The apparent QEs for formaldehyde and MeOH generation were calculated as four- and six-electron reactions, respectively.

Hongsen et al. propound the electrochemical reaction mechanism of oxidation for formaldehyde and/or MeOH over ordered intermetallic PtPb and pure Pt [12]. They suggest that formaldehyde and MeOH electrooxidations on PtPb and Pt produce different adsorbed substances as intermediates. When PtPb NPs are used as electrocatalysts for the oxidation of formaldehyde and MeOH, the oxidation pathway via CO_{ads} is precluded at all potentials. However, when Pt NPs are used as electrocatalysts, adsorbed CO is formed on the Pt surface from the dehydrogenation of formaldehyde and MeOH. Therefore, the enhanced photocatalytic performance of PtPb NPs/WO_3 was shown by the formation of ordered intermetallic compounds; PtPb NPs/WO_3 was more tolerant than Pt NPs CO poisoning when formaldehyde and/or MeOH were decomposed by the photocatalysts. These results show that the photocatalytic reaction mechanism for the decomposition of organic compounds was strongly dependent on the co-catalyst. Furthermore, it is probable that the oxidation of organic compounds in the photocatalytic decomposition occurred on the co-catalyst.

4. Conclusion

We have successfully synthesized WO_3-supported PtPb NPs using a photodeposition and polyol method. The XPS and TEM/STEM characterizations demonstrated that ordered intermetallic PtPb co-catalyst NPs were formed on the WO_3 surface. Furthermore, we demonstrated effective decomposition of various organic compounds over PtPb NPs/WO_3 compared with bare WO_3 and pure Pt NPs/WO_3. PtPb NPs/WO_3 exhibited enhanced photocatalytic activity toward various organic compounds. The reaction mechanism of the photocatalytic decomposition of various organic compounds was investigated. Higher photocatalytic activity was dependent on the co-catalyst. Both co-catalysts (Pt and PtPb NPs) showed different organic compound decomposition products (or chemisorbed species) and proceeded via different reaction pathways.

Acknowledgements

This work was financially supported by the Strategic Research Base Development Program for Private Universities of the 8Ministry of Education, Culture, Sports, Science and Technology of Japan.

A part of this work was supported by National Institute for Materials Science (NIMS) microstructural characterization platform as a program of “Nanotechnology Platform” of the Ministry of Education, Culture, Sports, Science and Technology (MEXT), Japan.

Appendix A. Supplementary data

Supplementary data associated with this article can be found, in the online version, at http://dx.doi.org/10.1016/j.apcatb.2015.08.016.

References

[1] (a) M.R. Hoffmann, S.T. Martin, W. Choi, D.W. Bahnemann, Chem. Rev. 95 (1995) 69–96;
(b) A. Fujishima, T.N. Rao, D.A.J. Tryk, Photochem. Photobiol. C 1 (2000) 1–12;
(c) H. Kisch, Angew. Chem. Int. Ed. 52 (2013) 812–847.
[2] A. Tanaka, K. Hashimoto, H.J. Kominami, J. Am. Chem. Soc. 136 (2014) 586–589.
[3] (a) K. Maeda, K.J. Domen, Phys. Chem. Lett. 1 (2010) 2655;
(b) E. Thimsen, F. Leformal, M. Graetzel, S.C. Warren, Nano Lett. 11 (2011) 35–43.
[4] K. Mori, H. Yamashita, M. Anpo, RSC Adv. 2 (2012) 3165–3172.
[5] T. Arai, M. Horiuchi, M. Yanagida, T. Gunji, H. Sugihara, K. Sayama, J. Phys. Chem. C 113 (2009) 6602–6609.
[6] T. Arai, M. Horiguchi, M. Yanagida, T. Gunji, H. Sugihara, K. Sayama, Chem. Commun. 43 (2008) 5565–5567.
[7] H.P. Maruska, A.K. Ghosh, Sol. Energy 20 (1978) 443–458.
[8] R. Abe, H. Takami, N. Murakami, B.J. Ohtani, J. Am. Chem. Soc. 130 (2008) 7780–7781.
[9] (a) F. Matsumoto, Electrochemistry 80 (2012) 132;
(b) F. Matsumoto, C. Roychowdhury, F.J. DiSalvo, H. Abruña, Electrochem. Soc. 155 (2008) B148–B154;
(c) T. Gunji, T. Tanabe, A.J. Jeevagan, S. Usui, T. Tsuda, S. Kaneko, G. Saravanan, H. Abe, F. Matsumoto, J. Power Sources 273 (2015) 990–998.
[10] T. Gunji, G. Saravanan, T. Tanabe, T. Tsuda, M. Miyauchi, G. Kobayashi, H. Abe, F. Matsumoto, Catal. Sci. Technol. 4 (2014) 1436–1445.
[11] T. Gunji, T. Tsuda, A.J. Jeevagan, M. Hashimoto, T. Tanabe, S. Kaneko, M. Miyauchi, G. Saravanan, H. Abe, F. Matsumoto, Catal. Commun. 56 (2014) 96–100.
[12] W. Hongsen, A. Laif, F.J. DiSalvo, H.D. Abruña, Phy. Chem. Chem. Phy. 10 (2008) 3739–3751.